A 5–780-MHz Transceiver ASIC for Multinuclear NMR Spectroscopy in 0.13- μ m BiCMOS

IEEE Transactions on Circuits and Systems I: Regular Papers

Dreyer, Frederik; Kruger, Daniel; Baas, Sander; Velders, Aldrik; Anders, Jens

https://doi.org/10.1109/TCSI.2023.3279495

A 5–780-MHz Transceiver ASIC for Multinuclear NMR Spectroscopy in 0.13-μm BiCMOS

Frederik Dreyer, *Graduate Student Member, IEEE*, Daniel Krüger, *Graduate Student Member, IEEE*, Sander Baas, Aldrik Velders, and Jens Anders, *Senior Member, IEEE*

***Abstract*— In this paper, we present a broadband (5-780 MHz) transceiver ASIC optimized for ^{1}H and X-nuclei nuclear magnetic resonance (NMR) with external custom-designed microcoils. The NMR-on-a-chip transceiver is realized in a 0.13 μm BiCMOS technology, consumes an area of 1100×900 μm^2, and integrates a quadrature receiver, consisting of a low-noise amplifier, a quadrature downconversion mixer, and intermediate-frequency variable gain amplifiers, a power amplifier, and a frequency synthesizer on a single chip. An extensive noise analysis of the BJT-based low-noise amplifier with regard to the optimum source impedance provides simplified expressions for an optimized LNA design for broadband NMR-on-a-chip applications. The NMR-on-chip transceiver provides a measured state-of-the-art input-referred voltage noise of 610 pV/$\sqrt{\text{Hz}}$ and a maximum RX gain of 66 dB. In combination with an external, custom-designed solenoidal microcoil, the presented NMR-on-a-chip transceiver achieves a state-of-the-art normalized ^{1}H spin sensitivity of 7.2×10^{17} spins/$\sqrt{\text{Hz}}$ · T^2/m with an untuned, i.e. broadband front-end. Proof of concept NMR experiments on multiple nuclei (^{1}H, ^{2}H, ^{13}C, and ^{19}F) verify the applicability of the proposed untuned, broadband approach.**

***Index Terms*— Nuclear magnetic resonance, NMR, NMR-on-a-chip, BiCMOS, transceiver, broadband, multi-nuclei.**

I. Introduction

NUCLEAR magnetic resonance (NMR) is an immensely powerful analytical technique for various applications ranging from chemistry to material sciences and medicine. This is mainly due to its unparalleled specificity as well as its complete non-invasiveness and non-destructiveness. Recently, heteronuclear (X-nuclei) NMR, i.e. NMR that in addition to classical single ^{1}H-NMR exploits information from multiple nuclei, such as ^{2}H, ^{13}C, and ^{19}F, is becoming increasingly important in the fields of chemistry, biology and medicine. It not only allows for a more detailed chemical analysis of a substance for e.g. drug discovery [1], but also in vitro and in vivo analysis of metabolites for e.g. personalized medicine [2]. Nevertheless, a major hurdle that still restrains NMR is its comparably low intrinsic signal-to-noise ratio (SNR), especially for mass- and volume limited samples. A promising strategy for improving the SNR is to use miniaturized NMR coils, which are adapted to the sample size [3], [4]. In conventional NMR systems, the readout electronics are placed outside the magnet, leading to a distance of up to several meters between the NMR coil and the first amplifier stage. To avoid reflections on the connecting cable, the impedance of the NMR coil needs to be tuned and matched to the characteristic impedance of the cable, typically 50 Ω, introducing an increased noise figure equal to the cable loss [5]. Moreover, the narrowband nature of conventional matching circuits renders the design of a broadband NMR receiver frontend challenging. Therefore, conventional multinuclear NMR experiments, which use the same detection coil for all nuclei, typically require multi-tuned coils [6] and complex electronic modules [7]. These limitations can be removed, by substituting the conventional NMR electronics with on-chip-NMR transceivers, and placing the NMR microcoil in close proximity to the transceiver [8], the whole NMR spectrometer can be put inside the magnetic field [9], [10], [11], [12], [13], [14], opening up new design degrees of freedom to preserve the intrinsic coil SNR with better energy efficiency.

In this paper, which is an extended version of [15], we present a broadband NMR-on-a-chip transceiver ASIC optimized for X-nuclei NMR spectroscopy with custom-designed solenoidal microcoils. A detailed noise analysis provides a guideline for an optimized LNA design for tuned and untuned broadband NMR-on-a-chip applications. The paper is organized as follows: Section II describes the NMR setup and methodology. In Section III a detailed noise analysis is carried out and simplified expressions for the design process are given. The NMR hardware, including the transceiver ASIC and the sensor front-end, is introduced in Section IV. Section V-B shows the electrical characterization, as well as proof-of-concept X-nuclei NMR measurements. Finally, we conclude the paper with a brief summary and a short outlook on future work in Section VI.

Manuscript received 2 November 2022; revised 28 March 2023; accepted 10 May 2023. Date of publication 2 June 2023; date of current version 30 August 2023. This work was supported in part by the DFG under Contract AN 984/10-1 (ScreeMR), in part by the BMBF under Contract 13N14809 (Nanospin), and in part by the Carl Zeiss Foundation. This article was recommended by Associate Editor R. Fontaine. *(Corresponding author: Frederik Dreyer.)*

Frederik Dreyer is with the Institute of Smart Sensors, University of Stuttgart, 70569 Stuttgart, Germany (e-mail: frederik.dreyer@iis.uni-stuttgart.de).

Daniel Krüger is with the Institute of Smart Sensors, University of Stuttgart, 70569 Stuttgart, Germany, and also with the John A. Paulson School of Engineering and Applied Sciences, Harvard University, Cambridge, MA 02138 USA.

Sander Baas and Aldrik Velders are with the Laboratory of BioNanoTechnology, Wageningen University, 6700 EK Wageningen, The Netherlands.

Jens Anders is with the Institute of Smart Sensors, University of Stuttgart, 70569 Stuttgart, Germany, also with the Institute for Microelectronics Stuttgart, IMS CHIPS, 70569 Stuttgart, Germany, and also with the Center for Integrated Quantum Science and Technology (IQST), 70569 Stuttgart, Germany.

Color versions of one or more figures in this article are available at https://doi.org/10.1109/TCSI.2023.3279495.

Digital Object Identifier 10.1109/TCSI.2023.3279495

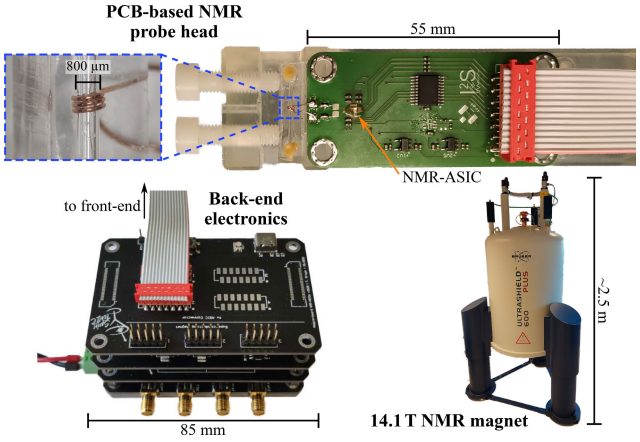

Fig. 1. Photographs of the main building blocks of the presented NMR spectroscopy system, including the NMR-on-a-chip transceiver, the custom-designed broadband NMR coil, the back-end electronics, and the 14.1 T NMR magnet.

II. NMR Setup and Methodology

Fig. 1 gives an overview of the measurement setup and its main building blocks. The corresponding block diagram, including the system architecture is presented in Fig. 8. The proposed system consists of a PCB-based NMR probe head, centered around an NMR-on-a-chip transceiver ASIC and a polydimethylsiloxane (PDMS) encapsulated broadband sensor coil, which is complemented by back-end electronics, including off-chip amplifiers and anti-aliasing filters (AAFs), driver- and buffer-stages, and a commercial data acquisition (DAQ) unit, which also controls the experiments. Post-processing of the recorded NMR data is performed on a computer using LabView (National Instruments) and MATLAB (Mathworks).

To conduct the NMR measurements in Section V-B, the whole PCB-based NMR front-end is placed in the bore of a commercial 14.1 T NMR magnet, cf. Fig. 1. The resulting Larmor frequencies are 600 MHz for protons (^{1}H), 565 MHz for fluoride (^{19}F), 151 MHz for carbon-13 (^{13}C), and 92 MHz for deuterium (^{2}H). The broadband NMR coil, described in detail in Section IV-B, is directly connected to the NMR-transceiver ASIC. Due to this close proximity, there is no need for the conventional 50-Ω-impedance matching, which in turn reduces the complexity of the RF frontend and allows for a more power-efficient receiver design [2]. Most in-field receivers presented in the literature [9], [10], [11], [13], [14], [16] use a capacitor in parallel to the NMR coil to form a parallel resonant circuit at the NMR frequency, which facilitates the design of the following LNA [15], [17], [18]. However, this approach limits the bandwidth of the RF frontend, preventing parallel X-nuclei experiments and requiring an adjustable tuning capacitance to perform time-multiplexed X-nuclei experiments. Therefore, it is, in principle, desirable to omit the tuning capacitor to enable true broadband operation, as it is proposed in this article. However, this places very stringent requirements on the LNA's noise performance, and we will provide a detailed noise analysis in Section III.

Fig. 2 shows an exemplary timing diagram of a time-multiplexed pulse sequence for two different nuclei. The advantage of such a heteronuclear experiment lies in the fact

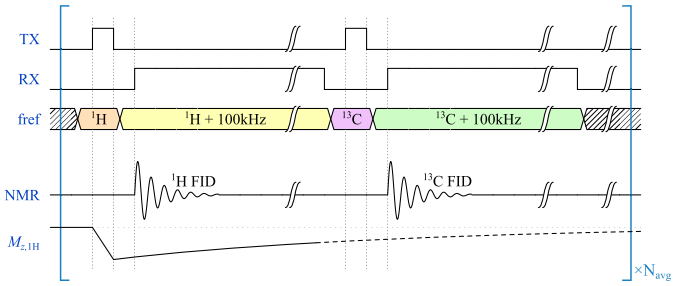

Fig. 2. Exemplary timing-diagram of a time-multiplexed X-nuclei NMR sequence for two different nuclei, here, ^{1}H and ^{13}C top illustrate how the second nucleus can already be excited and read out while the first nucleus is still relaxing back to its equilibrium magnetization along the B_0 axis.

that it is possible to excite a second nucleus while the first one is still relaxing back to its equilibrium magnetization along the B_0 axis, i.e., faster than a few longitudinal relaxation time constants of the first nucleus. The conceptual excitation scheme of Fig. 2 can easily be extended to a larger number of nuclei. Especially in the case of small ratios of transversal and longitudinal relaxation times, i.e., $T_2/T_1 \ll 1$, this quasi-parallel measurement of multiple nuclei can greatly speed up the overall measurement time and thereby improve the throughput of the system.

After the signal processing inside the NMR-ASIC, cf. Section IV-A for a detailed explanation, the low intermediate frequency (IF) output signals are post-processed off-chip by an active anti-aliasing filter (AAF) with a gain of 14 dB and a cut-off frequency of 250 kHz that drives the 2 MSps analog-to-digital converter (ADC) of the DAQ (National Instruments PXIe 6366).

A commercial arbitrary waveform generator (AWG) (Keysight 33612A) provides the reference frequency for the on-chip phase-locked loop (PLL), cf. Section IV-A, which generates the excitation waveform and the quadrature local oscillator (LO) signals. Phase-synchronous low-IF detection, which is, e. g., essential for NMR averaging experiments, is enabled by the frequency-shift keying (FSK) functionality of the Keysight 33612A [19]. With the FSK scheme, successive FIDs are phase synchronous because the FSK of the used AWG switches the frequency in a phase-continuous manner. This ensures that the FIDs before sampling are phase-synchronous. The timing of the pulses (TX, RX, and FSK) is controlled by the same DAQ hardware (NI PXIe-6366), which is also used for the digitization/sampling of the NMR signal. Therefore, although the clock signals of the ADC and the AWG output are not derived from a single reference, there is still a fixed phase relation between consecutive averages because the RX pulse defines a fixed phase for the sampling of the FID after each excitation pulse, i.e., the ADC sampling is synchronized to the RX pulse.

The ASIC's operating frequency and gain settings are programmed by an on-chip serial peripheral interface (SPI). All NMR experiments are orchestrated by a custom LabVIEW program that controls the NI DAQ device.

III. Noise Theory

NMR typically suffers from a weak intrinsic signal to noise ratio (SNR). Therefore it is essential that the electronics do not

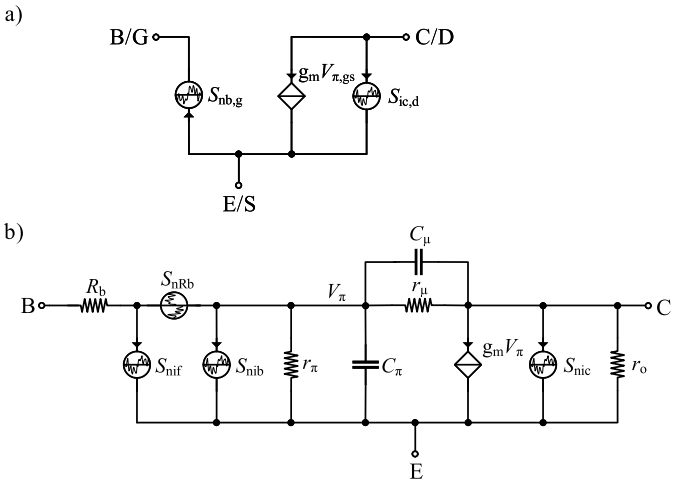

Fig. 3. a) Simplified noise model of both MOSFETs and BJTs and b) Hybrid-π noise model of a BJT.

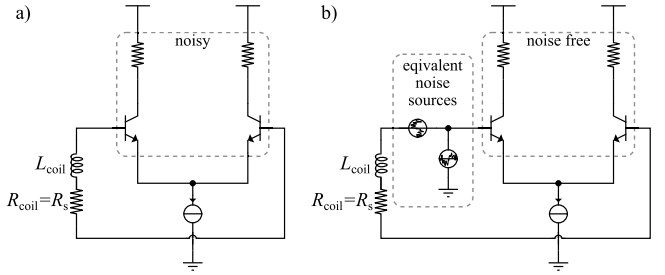

Fig. 4. a) Simplified noise model of a differential common-emitter LNA, and b) equivalent noise model of the LNA, representing the LNA noise with input-referred voltage and current noise sources.

further degrade the SNR of the NMR signal, and the thermal noise of the NMR coil should dominate the overall receiver noise. Here, the rms sensor coil noise is given by

$$n_{\text{coil}} = \sqrt{4kTR_{\text{L}}\Delta f}, \tag{1}$$

where k is the Boltzmann constant, T is the absolute coil temperature, R_{L} is the coil resistance, and Δf is the equivalent detection bandwidth. In typical chip-based NMR setups the sensor is tuned to a single Larmor frequency of a specific nucleus. This is achieved by forming a parallel resonant circuit between the NMR coil and a tuning capacitor. The effective input impedance, seen by the LNA is therefore purely resistive with typical values in the range of several kΩ, necessitating a high-impedance LNA input to avoid losses in the resulting voltage divider formed by the LC tank and the LNA input impedance.

The tuned configuration also leads to an effective detection bandwidth that is limited by the quality factor (Q) of the detection coil, preventing true broadband X-nuclear NMR experiments. Here, although it is, in principle, possible to use a tunable capacitor to switch between different Larmor frequencies, this setup still prevents a simultaneous readout of different Larmor frequencies. Therefore, an untuned, broadband readout of the NMR coil is very desirable. Here, as opposed to the tuned operation, the overall source impedance seen by the LNA is complex with its real part given by the AC coil resistance and its imaginary part given by the coil reactance ωL_{coil}, where L_{coil} is the coil inductance. Therefore, this configuration poses several challenges for the following LNA. First, the typically small coil resistance requires a very low input-referred voltage noise to enable a low noise figure (NF). Next, the input-referred current noise, which is present in both bipolar and MOS transistors, cf. Fig. 3a is converted into voltage noise by an impedance, whose value is increasing with frequency, further complicating the design of LNAs with low noise figures at higher operating frequencies.

In the following, we will provide a detailed noise analysis of the proposed broadband readout scheme. Here, it should be noted that the input-referred current noise of a BJT is frequency-independent whereas that of a MOSFET increases with frequency. This renders the design of very low-noise MOSFET LNAs at higher NMR operating frequencies for untuned coils, whose impedance also rises with frequency significantly, more challenging. Therefore, in the following, we will focus on LNAs incorporating BJTs as the first active element. The corresponding detailed noise model of a single BJT employed in this work is shown in Fig. 3b [20].

In this figure, B, E and C are the base, emitter, and collector terminals, R_{b} is the base resistance, r_π and C_π are the real- and imaginary part of the base-emitter impedance, respectively (imaginary part drawn as capacitance), r_μ and C_μ model the depletion zone between base and collector, g_{m} is the transconductance, and r_0 models the dynamic collector output resistance. The base resistance R_{b} generates thermal noise, which is represented by the noise density S_{nRb}. The base- and collector currents I_{b}, and I_{c} generate shot-noise, represented by the noise densities S_{nib}, and S_{nic}. Furthermore, the current passing through the base-emitter zone generates flicker-noise, which is represented by the noise density S_{nif}. Here, it should be noted that the equivalent small signal resistances r_π and and r_0 do not produce any noise. The noise generated by the NMR coil can be modeled according to Eq. (1). To simplify the following analysis, we will neglect r_μ and C_μ. This simplification results in greatly simplified analytical noise expressions. The simplified model can be justified by its good matching with transistor level simulations.

The power spectral density (PSD) of the thermal noise produced by the base resistance R_{b} is given by:

$$S_{\text{nRb}} = 4\ kT\,R_{\text{b}}. \tag{2}$$

The shot-noise due to I_{b}, and I_{c} is given by:

$$S_{\text{ni(b,c)}} = 2\ qI_{\text{(b,c)}}, \tag{3}$$

where q is the elementary charge.

The PSD of the noise voltage originating from the base-emitter current can be expressed as:

$$S_{\text{nif}}(f) = \frac{2qf_{\text{c}}I_{\text{b}}^{\gamma}R_{\text{b}}^2}{f}, \tag{4}$$

where f_{c} is the flicker-noise corner frequency, which, for BJTs, is typically in the range of a few kHz, and γ is a semi-empirical constant which depends on the carrier concentration in the channel and the device geometry. Typically γ is in the range of 0.5-1.

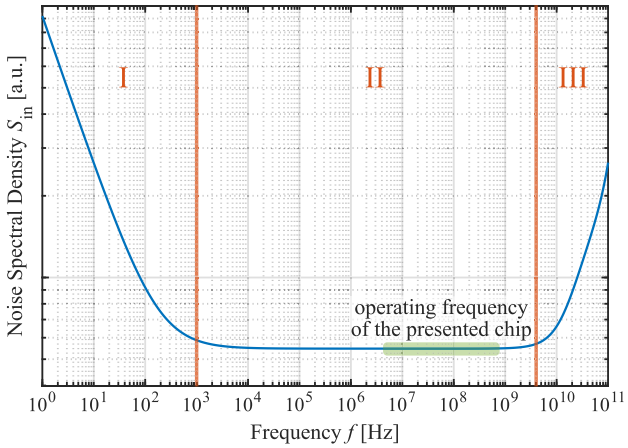

Fig. 5. Simulated total input-referred voltage noise of the LNA, displaying (I) a flicker-noise dominated region, (II) a flat mid-noise region, and (III) a region with a +20 dB/decade roll-off due to the roll-off in LNA gain, causing the LNA load resistors to increase the total input-referred noise. The simulation is performed for a source resistance of $R_s = 95\,\Omega$, i. e., the optimum source resistance of Fig. 7.

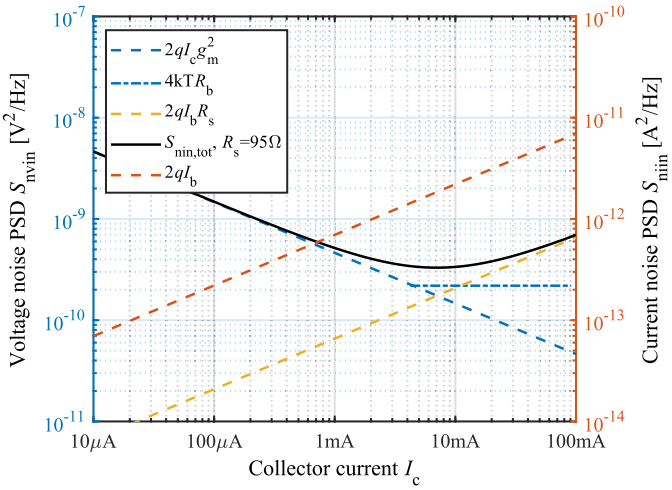

Fig. 6. Input-referred voltage- and current noise versus collector current.

Applying the noise model of Fig. 3b to the simplified LNA model of Fig. 4 and performing a conventional small signal noise analysis, we calculate the equivalent input-referred voltage and current noise of the differential bipolar common-emitter LNA employed in this work.

From this, we get an expression from which three dominant regions can be obtained, cf. Fig 5: I: for low frequencies the flicker-noise, which scales with $1/f$, is substantial, II: in the mid-band, the noise is more or less frequency independent, and therefore a minimum noise level can be obtained, and III: for high frequencies, the LNA gain rolls off, causing the noise of the load resistors to contribute more and more to the total input-referred noise.

As can be seen from Fig. 5, the intended operating region of 5-600 MHz, where the upper frequency corresponds to the proton Larmor frequency of a 14.1 T magnet, lies in region II, which omits the low-frequency flicker-noise as well as the increase in noise due to the roll-off of the LNA gain.

Neglecting the contribution from the source resistance R_s, the PSD of the equivalent input-referred voltage noise calculates to:

$$S_{nvin} = 4\ kT\,R_b + 2\ qI_bR_b^2 + \frac{2qI_cr_\pi^2}{\beta^2} + 2\ qI_cR_b^2\left(\frac{f}{f_t}\right), \tag{5}$$

where f_T is the transit frequency. With $R_b^2 \ll r_\pi/g_m$, $r_\pi = \beta/g_m$, and $g_m = qI_c/kT$, Eq. (5) can be further simplified to:

$$S_{nvin} = 4\ kT\,R_b + 2\ q\frac{I_c}{g_m^2} + I_cR_b^2\left(\frac{f}{f_t}\right). \tag{6}$$

Again neglecting the contribution from the source resistance R_s, the PSD of the equivalent input-referred current noise is given by:

$$S_{niin} = 2\ qI_b + \frac{2qI_c}{\beta^2} + 2\ qI_c\left(\frac{f}{f_t}\right)^2. \tag{7}$$

Eq, (7) can be further simplified assuming a sufficiently large current gain β and a sufficiently small ratio of (f/f_t), resulting in a simplified PSD of the input-referred current noise according to:

$$S_{niin} = 2\ qI_b. \tag{8}$$

Since the simplified expressions for the input-referred voltage and current noise in Eqs. (6) and (8) are uncorrelated, we can write the PSD of the total input referred voltage noise for a real-valued source impedance R_s according to:

$$S_{nin,tot} = S_{nvin} + S_{niin}R_s^2 + 4\ kT\,R_s. \tag{9}$$

According to Eq. (9), for small values of the source resistance R_s the voltage noise is dominant whereas for large values of R_s the current noise becomes dominant. Fig. 6 plots the individual noise contributions as a function of the collector current. According to the figure, for small values of I_c, the input-referred voltage noise dominates. By contrast, for sufficiently large values of I_c, the input-referred current noise becomes the dominant noise contributor. In between, for each value of R_s, cf. the black line for $R_s = 95\,\Omega$, there is an optimum value of I_c, for which the contributions from the input-referred voltage and current noise are (nearly) equal. Considering only simplified expressions for the voltage and current noise according to

$$S_{nvin} = 2q\frac{I_C}{g_m^2} \tag{10}$$

and

$$S_{niin} = 2qI_B \tag{11}$$

this optimum collector current is, for a given source resistance R_s, given by

$$I_{c,opt} = \sqrt{\beta}\frac{V_t}{R_s}, \tag{12}$$

where $V_t = kT/q$ is the thermal voltage.

From Eq. (9) and using the simplified noise expressions above, we can derive an expression for noise factor as a

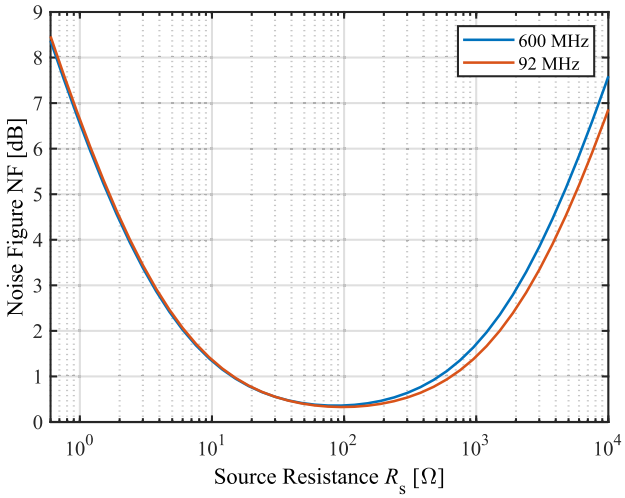

Fig. 7. Noise figure versus source resistance R_s for two different operating frequencies.

function of the (real-valued) source resistance R_s, which is given by:

$$F = 1 + \frac{2qI_c/g_m^2 + R_s^2 \cdot 2qI_b}{4\ kT R_s}. \tag{13}$$

Clearly, for small values of R_s, the input-referred collector current is dominant whereas for larger values of R_s the base current is the important noise contributor. Consequently, there is an optimum value for R_s for which the contributions from the collector and the base current are (nearly) equal. This optimum source resistance can be calculated as:

$$R_{s,opt} = \sqrt{\beta}\frac{V_t}{I_c}. \tag{14}$$

Eqs. (12) and (14) clearly indicate that for a given source resistance, there is an optimum collector current and vice versa. Here, in general, smaller resistance values require larger collector currents, explaining why the tuned approach, which results in equivalent tank resistance between a few hundred Ω and a few kΩ, greatly relaxed the required power budget for the LNA. By contrast, trying to read out a conventional NMR coil with typical resistance values of only a few hundreds of mΩ would require excessively large currents. Here, it should be noted that for a coil the actual source impedance is given by $R_s + jX_s$ with $X_s \gg R_s$, slightly modifying Eq. (9) but not changing any of the general conclusions drawn above.

As an important conclusion from the above noise analysis, when designing a broadband NMR system, the designer should employ a co-design between the coil and the LNA, trying to maximize the coil resistance for a given operating frequency, i.e. minimum coil self-resonance frequency. This results in an acceptable required power budget for the LNA and, at the same time, an acceptable noise performance.

To verify the presented noise model, we have run post-layout simulations of the LNA employed in the presented NMR transceiver. Fig. 7 shows the NF for this LNA as a function of the (real-valued) source resistance R_s for two operating frequencies of 600 MHz and 92 MHz, respectively. According to the figure, with its nominal collector current of $I_c = 8$ mA, the presented LNA provides an optimum noise performance for a source resistance of $R_s = 96\,\Omega$, which matches very well with the presented theory. The theoretically predicted value is 80 Ω (for $\beta = 600$). Moreover, the presented LNA provides a very good noise performance below 2 dB for source resistances between 6 Ω and approximately 1.5 kΩ, rendering it suitable both for the readout of tuned coils and optimized, multi-turn solenoidal NMR coils with relatively large coil resistances.

IV. NMR Hardware

The block diagram of the proposed broadband NMR system is shown in Fig. 8. It consists of three main building blocks: the on-chip NMR transceiver ASIC, the miniaturized broadband coil, incl. an optional tuning capacitor, as well as the back-end electronics for data acquisition and experiment control.

A. Transceiver ASIC

The colored rectangle inside Fig. 8 displays the architecture of the NMR-on-a-chip transceiver ASIC. The three main building blocks are the on-chip frequency synthesizer (blue), the transmitter (yellow), and the quadrature receiver (green). Besides that, the ASIC also incorporates a programmable beta multiplier current reference circuit, as well as an SPI, which can be used to program the frequency multiplication factor of the frequency synthesizer, the receiver gain, the reference current, and to trigger an automatic offset compensation. The programmable beta multiplier is designed for a nominal reference current of 100 µA with a tuning range of ±20 %, which can be used to vary the internal bias current of the LNA, which helps to compensate for process variations, and to adapt the LNA to its connected input impedance, cf. Section III.

1) Frequency Synthesizer: Depending on the actual B_0-field strength, the frequency synthesis block of a high-field, broadband NMR transceiver needs to provide operating frequencies between a few MHz and a few hundred MHz. In this work, we used a magnetic field of $B_0 = 14.1$ T, resulting in operating frequencies ranging from ∼10 MHz (^{191}Ir) to 600 MHz (^{1}H). To provide this relatively large range of frequencies for both the transmitter, as well as the quadrature receiver, we implemented a PLL-based frequency synthesizer that incorporates a ring-oscillator voltage-controlled oscillator (VCO) to generate the different NMR frequencies from a low-frequency reference. Here, a low-frequency reference signal is desirable, as it is compatible with flatband cables and does not require dedicated shielded RF cables running into the magnet.

The architecture of the on-chip frequency synthesizer is shown in Fig. 9. It uses a second-order integer-N PLL with programmable frequency-divider output and a pseudo-differential divide-by-2 IQ generator, which drives both the transmitter and the quadrature receiver. Here, an integer-N architecture has been chosen because the PLL needs a relatively large loop bandwidth of 600 kHz to enable fast settling for the FSK scheme mentioned above. This relatively large bandwidth renders the design of a low-phase-noise fractional PLL somewhat challenging. The voltage-controlled oscillator (VCO) is designed as a current-starved ring oscillator to maximize its tuning range. According to the figure, the PLL

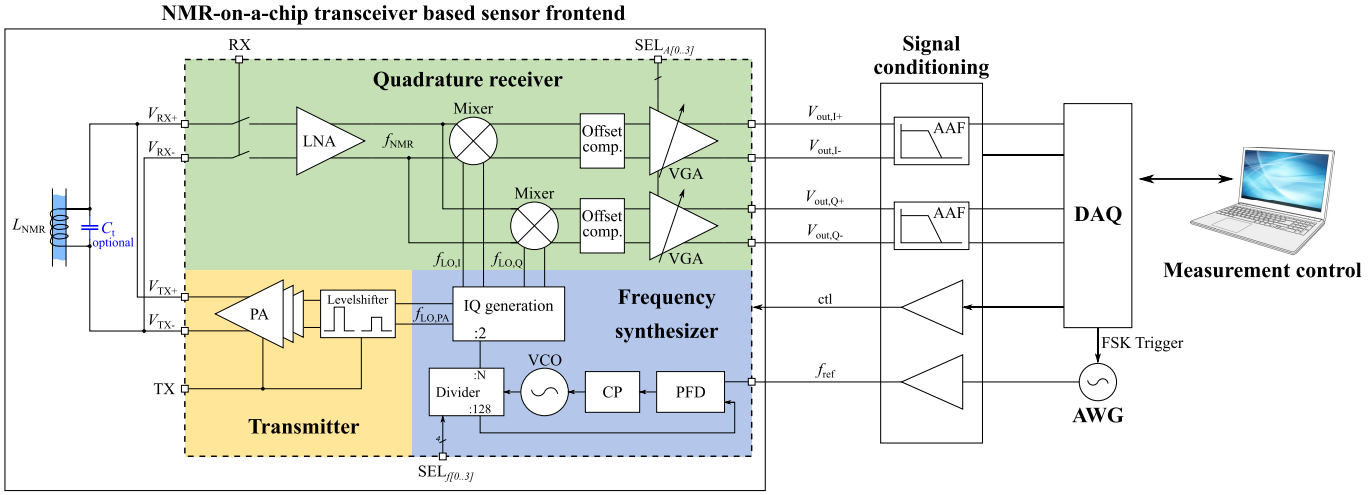

Fig. 8. Block diagram of the NMR front-end, including the architecture of the NMR-on-a-chip transceiver.

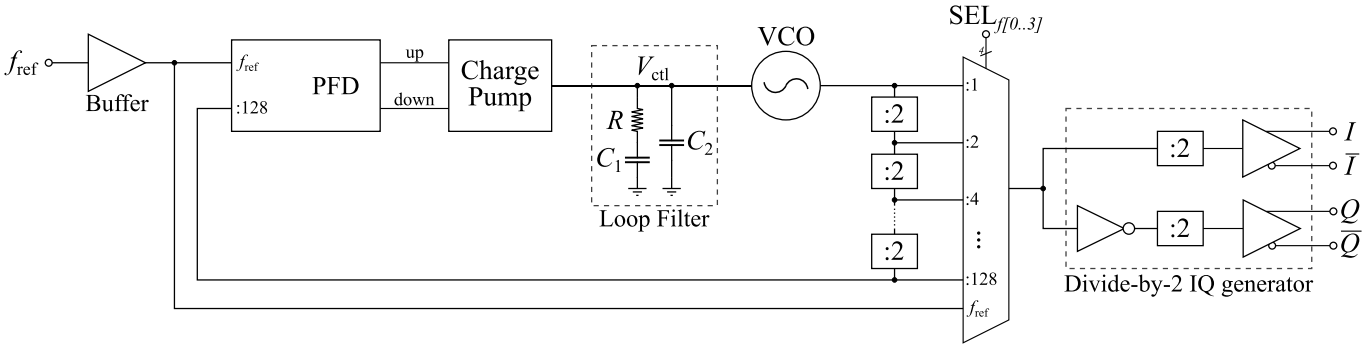

Fig. 9. Block diagram of the frequency synthesizer, including the phase-locked loop, the programmable output frequency divider, and the pseudo-differential divide-by-2 IQ generator.

uses a fixed PLL divider ratio of $N_{\mathrm{PLL}} = 128$, causing the VCO to operate at 128 times the reference frequency. Therefore, we have to use the external reference frequency to fine-tune the output of the frequency synthesizer to the exact target Larmor frequency of the nucleus of interest. To increase the operating range of the frequency synthesizer towards the lower end without the need for an ultra-wide tuning range VCO, we use a programmable frequency divider at the output of the PLL-based frequency synthesizer, realized by an analog multiplexer that can tap different stages of the divide-by-128 frequency divider to provide a programmable LO division factor $N_{\mathrm{div,out}}$ of up to 128. In this way, we limit the range of required reference frequencies, which eases the requirements on the needed reference frequency generator, while, at the same time, not deteriorating the noise performance. Further, it is possible to bridge the PLL and directly drive the multiplexer with the external reference frequency to extend the operating range to even lower frequencies. The multiplexer output signal is then fed into a divide-by-2 IQ generator, cf. Fig. 9. The IQ generator provides two 90Â°-phase-shifted, pseudo-differential output signals (I and Q), which are needed to drive the quadrature down-conversion mixer of the receiver path. The I channel outputs are further used to drive the transmitter.

2) Transmitter: The transmitter provides the amplified RF signal that excites the nuclear spins. It consists of a power amplifier (PA) with an H-bridge output, which is driven by a level shifter and predrivers, cf. [9], [21]. The PA is based on the architecture described in [21] and uses the pseudo-differential outputs from the frequency synthesizer to enable a differential driving of the NMR coil. More specifically, the PLL outputs are first level shifted from the core voltage of 1.2 V to the PA supply voltage of 2.5 V. The output of the inverting level-shifter connects to a chain of six scaled inverters with increasing driving strength, which drives the large transistors of the H-bridge while keeping the overall delay of the tapered buffer to a minimum.

In the receive mode, the output of the PA is switched to a high-impedance state, to avoid a distortion of the received NMR signal. As suggested in [21], the high impedance state is achieved by setting the output of the driver chain to a logic "1" to disable the PMOS transistor, disconnecting the gate of the NMOS from the driver chain by a transmission gate and shorting its input to ground to bring both transistors into a high-ohmic state.

3) Quadrature Receiver: The receiver chain of the NMR ASIC uses a conventional low-IF architecture, consisting of a low noise amplifier (LNA) followed by quadrature downconversion mixers and two digitally programmable variable gain amplifiers (VGAs) with automatic offset compensation.

Given the very weak intrinsic SNR of the NMR signal, according to the Friis formula, besides an excellent noise

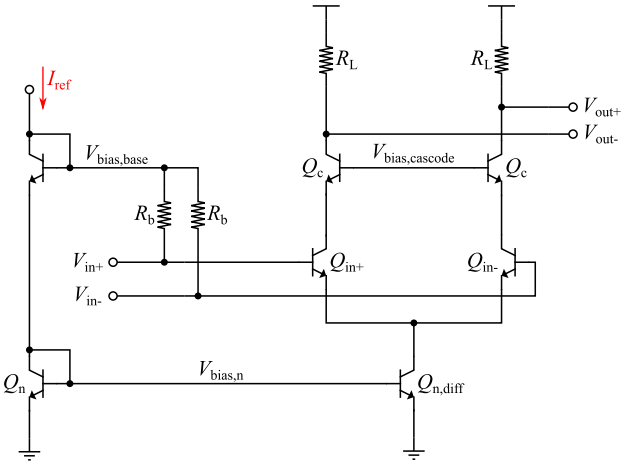

Fig. 10. Schematic of the LNA with a cascoded BJT input stage and resistive loads.

performance, cf. Section III, the LNA must also provide sufficient gain to mitigate the noise contribution of the subsequent stages. Therefore, in the presented chip, we use a fully-differential cascoded common emitter amplifier with resistive loads, cf. Fig. 10. This topology can provide very low noise over a large bandwidth, while delivering sufficient gain to suppress the noise contribution of the following stages. In addition, the cascoding greatly reduces the Miller effect and, therefore, the effective input capacitance of the LNA, which is important to avoid a parasitic tuning of the NMR coil by the LNA.

The LNA output signal is then down-converted to an IF of around 100 kHz, by using an AC coupled CMOS-based Gilbert-cell low-IF quadrature down-conversion mixers. Compared to a simple down-conversion mixer, the quadrature architecture provides a 3-dB-improved single-sideband receiver noise figure (NF), and it allows for both homodyne and low-IF detection. The former benefits from the intrinsically coherent output phase across different scans but introduces a trade-off between excitation efficiency – on-resonance excitation allows for a more efficient spin excitation than off-resonance excitation – and $1/f$-noise – for a single spectral line, on-resonance excitation results in zero IF, while off-resonance excitation produces a small non-zero IF, cf. [22]. On the other hand, a low-IF operation mitigates or even removes the $1/f$-noise problem but requires dedicated measures to ensure phase coherence in the detected NMR signals between successive pulses [22]. As mentioned above, in this work, we decided to use a reference generator for the PLL-based frequency generator that ensures phase coherence by switching between the excitation and detection reference frequencies at zero phase.

The mixers are driven by the quadrature outputs of the frequency generator. Due to mismatch inside the mixers and parasitic coupling of the LO signals to the mixer inputs, the down-converted output signals can be affected by a DC offset. Especially for higher operating frequencies, the stronger capacitive parasitic coupling can lead to large DC offsets of a few tens of millivolts that greatly reduce the overall dynamic range of the receiver. Since a simple AC coupling would result in large deadtimes after each excitation pulse [10], we introduced an automatic offset compensation circuit similar to the one presented in [23] at the output of the mixers.

The offset-compensated mixer output signals are then further amplified by two VGAs. The VGAs are implemented as fully-differential amplifiers with a driving strength of around 25 pF, which in turn allows for directly driving the several-meter-long interconnection cables ($l \leq 10$ m) between the ASIC and the back-end electronics outside of the magnet. Furthermore, the VGAs feature a 4-bit programmable gain between 0 dB and 34 dB to optimally adapt the gain and dynamic range of the overall receiver chain to a variety of different samples.

B. Broadband NMR Sensor Front-End

The broadband NMR sensor front-end (cf. Fig. 1) consists of a PCB, which carries the on-chip NMR transceiver ASIC, see Section IV-A, digital buffers for signal conditioning, and low-dropout regulators (LDOs) to generate the supply voltages for the ASIC. The PCB connects to a closely-spaced broadband NMR coil, whose design is similar to the ones presented in [24] and [25]. More specifically, the coil is implemented as a 3-turn solenoid wound around a glass capillary (1 mm OD, 0.8 mm ID) embedded in PDMS to form a microfluidic sample channel. A photograph of this assembly is shown in Fig. 1. While miniaturized NMR coils are key-enablers for the study of mass-limited samples, their fabrication is often relatively time-consuming and complex. Making use of such simplified and polymer-based microfluidic NMR devices with fast and low-cost fabrication, as it is done in this work, helps in overcoming these drawbacks [25]. In addition, such microcoils bring with them further advantages: with the option of manufacturing a coil with such a precision, the coil volume can be designed to match the sample volume, which in turn maximizes the SNR of the NMR signal [3]. Furthermore, the custom multiturn solenoidal coils can be implemented with a coil impedance that matches – or is at least close to – the optimum source impedance derived in Section III, to optimize the overall system NF. With a total length of 600 µm and an inner diameter of 800 µm the effective sample volume is approximately 300 nl. For a detailed characterization of the NMR coil see Section V-A.

V. Chip Implementation and Measurements

The die photograph of the manufactured NMR transceiver ASIC with highlighted building blocks is shown in Fig. 11. The ASIC occupies a total chip area of $1100 \times 900\,\mu m^2$ and is fabricated in a 0.13 µm SiGe BiCMOS technology.

To demonstrate the versatility and excellent performance of the presented on-chip NMR system, we first performed an electrical characterization of both the NMR ASIC and the broadband sensor followed by broadband NMR measurements on various different nuclei.

A. Electrical Characterization

For the initial electrical characterization of the NMR-on-a-chip ASIC [15], we first measured the conversion gain of

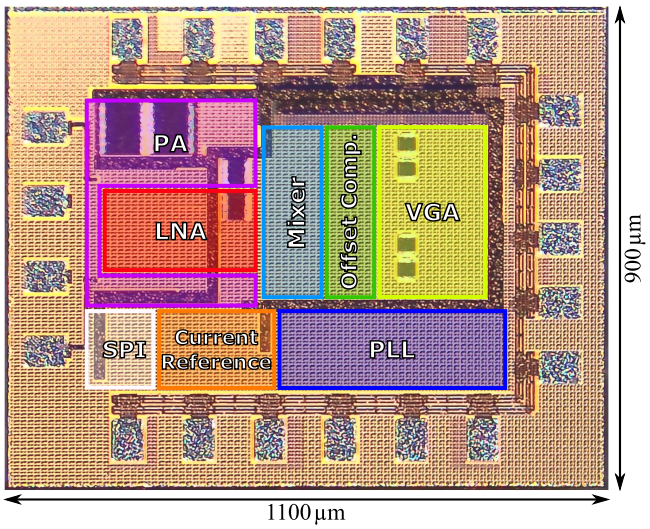

Fig. 11. Die micrograph of the presented NMR transceiver ASIC with annotated building blocks.

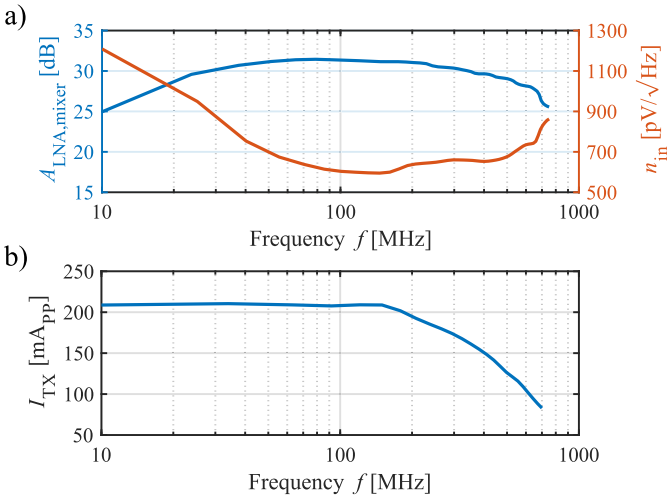

Fig. 12. a) Conversion gain $A_{\mathrm{LNA,mixer}}$ of the LNA-mixer-combination and input-referred noise n_{in} of the LNA, and b) peak-to-peak output current I_{TX} of the PA into a 10 Ω load resistor as a function of frequency.

the quadrature receiver. To do so, we fed a differential RF signal into the 100 Ω terminated input of the ASIC using a signal generator (Rohde & Schwarz SMA100B) and a 180°-powersplitter (Mini-Circuits ZFSCJ-2-1-S+). By setting the gain of the VGA to 0 dB and measuring the chip output signal using a signal analyzer (Rohde & Schwarz FSV), we determined a maximum conversion gain of the LNA-mixer combination of 31.5 dB, see Fig. 12a. Here, the roll-off in conversion below the lower corner frequency of approximately 20 MHz originates from the AC coupling between the LNA and the down-conversion mixers. This corner frequency was chosen as a compromise between chip area and operating range of the presented NMR-on-a-chip transceiver, considering the chip's main application of high-field/high-frequency X-nuclei NMR. Subsequently, we experimentally verified the 4-bit controllable VGA gain range between 0 dB and 34 dB.

Next, to verify the noise model presented in Section III, we measured the effect of different source resistances on the

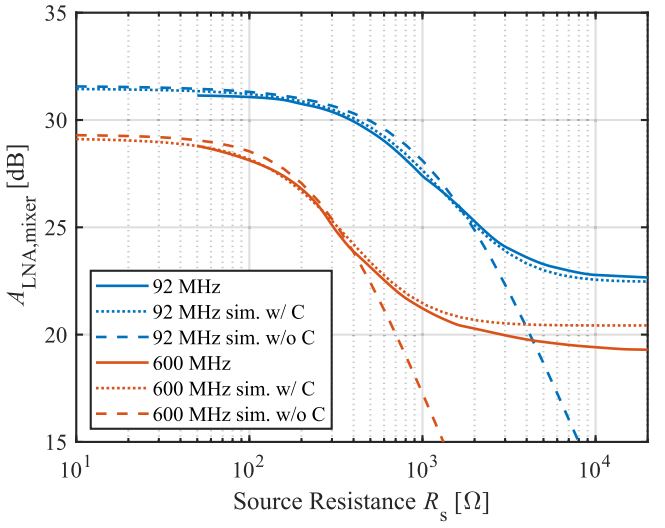

Fig. 13. Measured and simulated conversion gain $A_{\mathrm{LNA,mixer}}$ of the LNA-mixer-combination versus the source resistance R_{s}. To match the simulation to the measurement, in the simulations, we added a 350 fF capacitor in parallel to the source resistance R_{s}.

receiver gain by driving the presented BJT-LNA with a variable series source resistance R_{s}. Here, it should be noted, that, in the actual NMR setup, the source impedance in the tuned case is given by $Q^2 \cdot R_{\mathrm{L}}$ (resistive) and $Q \cdot R_{\mathrm{L}}$ (inductive) for the untuned case. Fig. 13 compares the measured conversion gain of the LNA-mixer-combination to the simulated values versus R_{s} for frequencies of 600 MHz and 92 MHz. Here it can be seen that for increasing values of R_{s} the maximum achievable gain of the input stage drops significantly before reaching a plateau for $R_{\mathrm{s}} > 10\,\mathrm{k\Omega}$. This plateau for larger source resistances is due to the parasitic capacitance of the utilized discrete source resistors. In simulations we were able to mimic this effect by adding a 350 fF capacitor in parallel to the ohmic resistor, which, for higher source resistances R_{s}, forms a capacitive voltage divider with the LNA input capacitance. As can be seen from the figure, for source resistances up to the optimum value of around 100 Ω (cf. Section III), the LNA provides the maximum amplification of 27 dB and 31.5 dB respectively, whereas for large source resistances beyond a few kΩ, the gain significantly decreases. This effect is of particular importance for tuned readouts with high quality factor coils.

Further, it should be noted, that the decrease in gain with increasing source resistances is particularly important for BJT LNAs, as utilized in this work, due to their comparably low input impedance. By contrast, CMOS LNAs typically display a much higher input impedance, which is dominated by the gate-source capacitance. This being said, especially for large bias currents, operation deep in weak inversion and parallel-tuned NMR coils, the large gate capacitance in combination with the large source impedance associated with these conditions can also introduce a significant voltage division at the input of CMOS LNAs.

In addition, we have measured the complex output voltage noise by combining the I and Q channels into a complex signal for a shorted LNA input, using the same signal analyzer at a constant offset frequency of $f_{\mathrm{IF}} = 100\,\mathrm{kHz}$. From this result,

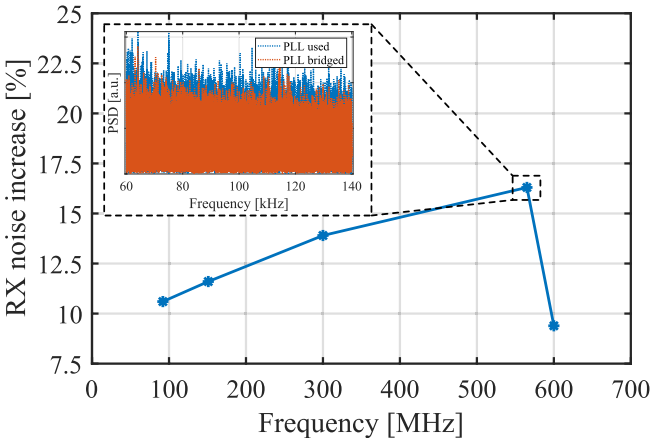

Fig. 14. Increase in receiver noise due to the use of the on-chip PLL compared to an ultra-low noise external signal generator as the LO signal for the mixer.

we calculated the input-referred voltage noise S_{nvin} by dividing the output-referred noise by the previously measured conversion gain. The measured input-referred noise PSD as a function of RF frequency is shown in Fig. 12a. According to the plot, the input-referred voltage noise stays below $700\,\text{pV}/\sqrt{\text{Hz}}$ for frequencies between 50 MHz and 550 MHz with a minimum of $610\,\text{pV}/\sqrt{\text{Hz}}$, which corresponds to a deviation of less than 10 % compared to post-layout simulations. As explained in Section III, due to the use of a BJT-based LNA input stage, the contribution of the input-referred current noise cannot be neglected. Especially for a high input impedance, as they are, e.g. associated with tuned NMR probe heads, the overall receiver NF can be dominated by the input-referred current noise. Therefore, we have measured the in-band 50 Ω NF of the LNA, by using a noise source (Noisecom NC346B) and the FSW-K30 option of the signal analyzer. In this way, we measured a receiver NF of 1.8 dB for a high input impedance, which was verified by the Y factor method [18]. Starting from the measured NF and the Y-parameters of the LNA, we calculated an input-referred current noise of $1.7\,\text{pA}/\sqrt{\text{Hz}}$. Compared to post-layout simulations, this corresponds to a deviation of less than 15 %. Additionally, we determined the phase imbalance ϕ_e of the quadrature receiver between the I and the Q channel according to [26]:

$$\phi_e = \frac{2}{\sqrt{\left(\frac{\hat{x}_{\text{sig}}}{\hat{x}_{\text{leak}}}\right)^2 - 1}}, \tag{15}$$

where $\hat{x}_{\text{sig}}$ is the measured signal intensity at the down-converted frequency $\Delta\omega = \omega_{\text{RF}} - \omega_{\text{LO}}$ and $\hat{x}_{\text{leak}}$ is the undesired leakage signal at the inverse image frequency $-\Delta\omega$. In this way, we calculated a maximum phase imbalance ϕ_e of 0.9°, corresponding to a minimum image rejection ratio of 42 dB, and a degradation of the receiver NF of less than 0.01 dB.

Next, we measured the noise contribution of the PLL on the overall RX noise. Here, we compared the output noise spectrum of the ASIC for the two cases of (i) using the on-chip PLL and (ii) bridging the PLL and using an ultra-low-noise external frequency synthesizer (Rohde & Schwarz SMB100B) as LO signal for the mixer. This comparison was performed for a wide range of LO frequencies over an IF bandwidth of 80 kHz centered around an IF of 100 kHz. Fig. 14 shows that the on-chip PLL produces a slightly increase receiver noise with the increase in noise ranging from 9 to 16% over the frequency range from 90 to 600 MHz.

After the characterization of the receiver, we analyzed the transmitter. Here, we first measured the maximum output current into a 10 Ω load resistor. Fig. 12b shows the corresponding maximum peak-to-peak output current I_{TX} as a function of frequency. As can be seen from this plot, the PA delivers a maximum current of 210 mA for output frequencies up to 130 MHz. For higher frequencies the current decreases with a roll-off of approximately 3 dB per octave.

By tracking the PA output frequency we measured the PLL lock range to extend from reference frequencies of 5.5 MHz to 12.2 MHz, corresponding to LO frequencies between 710 MHz and 1.56 GHz. Due to the programmable frequency divider and the option to bridge the PLL, cf. Section IV-A, the proposed NMR system can operate over a wide frequency range from 5 MHz up to 780 MHz, where the lower limit is defined by on-chip AC coupling capacitors between the LNA and the mixers, which lead to a drop in the receiver gain and therefore an increase in the input-referred noise for low frequencies, see Fig. 12.

Before conducting the NMR measurements of the following section, we have also characterized the custom-built microcoil electrically. At 600 MHz the microcoil displays an inductance of $L = 24$ nH, and an effective series resistance of $R_{\text{L}} = 2\,\Omega$. For a tuned operation, by forming a parallel resonant circuit in combination with a capacitance of 3 pF, the equivalent source impedance is 5.5 kΩ.

B. NMR Measurements

To validate the presented NMR setup in its target application, we performed different single-pulse NMR experiments on different nuclei with the NMR system described in Section II.

To this end, we first characterized the minimal achievable dead-time due to the ring-down of the energy stored inside the NMR coil between the TX pulse and the start of the acquisition. In the tuned case, the dead-time is around 400 ns for frequencies up to 100 MHz. For higher frequencies, due to the shorter oscillation periods, the dead-time decreases with a minimum dead-time in the tuned case of 200 ns at a frequency of 600 MHz. For the untuned NMR coil, the absence of a tuned LC resonator drastically reduces the intrinsic dead-time to less than 15 ns over the whole frequency range. However, due to the limited settling speed of the PLL after a frequency hop, in the case of an untuned NMR coil and the use of the FSK scheme with an IF of 100 kHz, the actual dead-time is limited by the PLL settling time of approximately 100 ns.

As explained in [15], the PDMS encapsulation around the NMR sensor coil causes the ^{1}H-NMR signal of the analyte to be superimposed by a broad peak. In contrast to the compensation technique presented in [15], in this work, we used a simple pre-acquisition delay between the TX pulse and the start of the data acquisition of 4 ms for all proton measurements. In this way, the NMR signal of the solid PDMS has already decayed

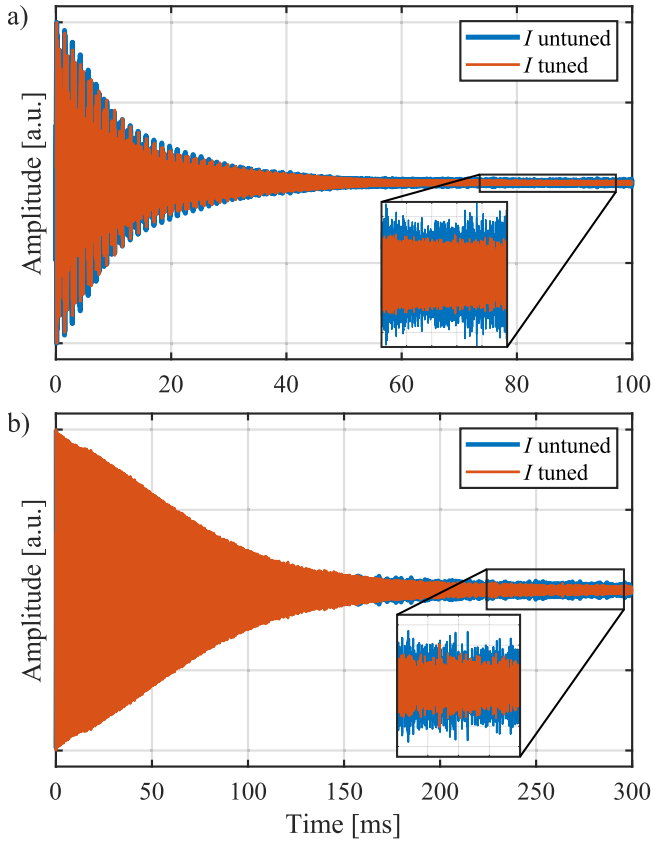

Fig. 15. Normalized FIDs of a) a proton NMR experiment of an ethanol sample and b) a deuterium NMR experiment of a D_2O sample, measured with both an untuned (blue) and a tuned (red) NMR coil.

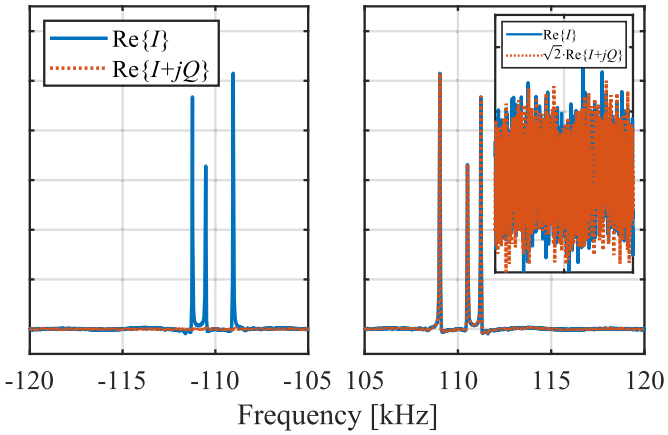

Fig. 16. Normalized ^{1}H frequency spectra of an ethanol sample of the complex FID vs. the in-phase FID.

TABLE I
MEASURED AND SIMULATED SNR REDUCTION FROM THE TUNED TO THE UNTUNED CASE FOR DIFFERENT NUCLEI

Nucleus	^{1}H	^{2}H	^{13}C	^{19}F
Measured SNR reduction [%]	25 - 33	25 - 30	N/A	N/A
Simulated SNR reduction [%]	31	27	34	31

to zero by the time the data acquisition is started, and only a relatively small fraction of the much longer-lived liquid-state signals are truncated.

As our first NMR experiment, we performed benchmark proton measurements on a 300 nl ethanol sample with both the tuned as well as the untuned NMR front-end in order to compare the performance of the two approaches. Fig. 15a shows the free induction decay (FID) for the two recorded ethanol signals. For better comparability, we normalized the initial amplitudes to one.

From these data, we extracted the time-domain SNR, SNR_t, by measuring the maximum NMR signal, $\hat{x}_{\mathrm{NMR}}$, at the beginning of the real-valued in-phase FID and measuring the noise spectral density after 1 s of measurement time, i. e. waiting until the NMR signal has completely decayed. To quantify the noise spectral density, we measured the rms value from the in-phase time domain trace and divided it by the equivalent noise bandwidth, taking into account the improvement of $\sqrt{2}$ offered by the quadrature detection to obtain the noise spectral density N_{noise}. The time-domain SNR is then defined as $\hat{x}_{\mathrm{NMR}}/N_{\mathrm{noise}}$. We also verified the noise improvement by a factor of $\sqrt{2}$ in the real part of the FFT of the complex FID vs. that of the in-phase FID only, see Fig. 16.

Applying this procedure, we found that the extracted SNR of the tuned measurement is about 25-33% better than that of the untuned measurement.

From the time-domain SNR, we calculated the time-domain ^{1}H spin sensitivities according to $N_{\mathrm{min}} = 3 \cdot \mathrm{SNR}_t/N_{\mathrm{spins}}$, where N_{spins} is the number of spins inside the sample. In this way, we measured spin sensitivities of $N_{\mathrm{min,untuned}} = 3.46 \times 10^{12}\,\mathrm{spins}/\sqrt{\mathrm{Hz}}$ for the untuned coil and $N_{\mathrm{min,tuned}} = 2.59 \times 10^{12}\,\mathrm{spins}/\sqrt{\mathrm{Hz}}$ for the tuned coil. From these values it is clearly visible that, as predicted by the theoretical noise analysis in Section III, there is only a slight decrease in performance between the tuned and the untuned readout. The 30 % SNR drop could be compensated by averaging over 1.7 times increased measurement time.

To demonstrate the enhanced flexibility of the untuned probe head, we then performed NMR experiments on various other nuclei, namely ^{2}H, ^{13}C, and ^{19}F.

As for the proton experiments, Fig. 15b shows the tuned and untuned FIDs of a ^{2}H NMR measurement of a D_2O sample. A comparison of the SNR performance of the tuned vs. the untuned measurements for all the different nuclei is given in Table I. As can be seen from the table, the reduction in SNR stays in the range of 25 to 35% for all four nuclei. Here, it should be noted that the SNR reductions for the ^{13}C and ^{19}F nuclei are extracted from simulations that take into account the measured coil parameters as well as the equivalent series resistance (ESR) of the used tuning capacitors in a Virtuoso testbench of the LNA. This simulation-based approach can be justified by the fact that the simulations for the ^{1}H and ^{2}H nuclei matched within a few percent with the measured data.

Further, Fig. 17 shows the corresponding NMR spectra measured with the untuned sensor front-end. The data were first order phase corrected (a constant phase correction and a linear-with-frequency phase correction). The minimum linewidth of the NMR spectra after shimming was 40 ppb. As samples

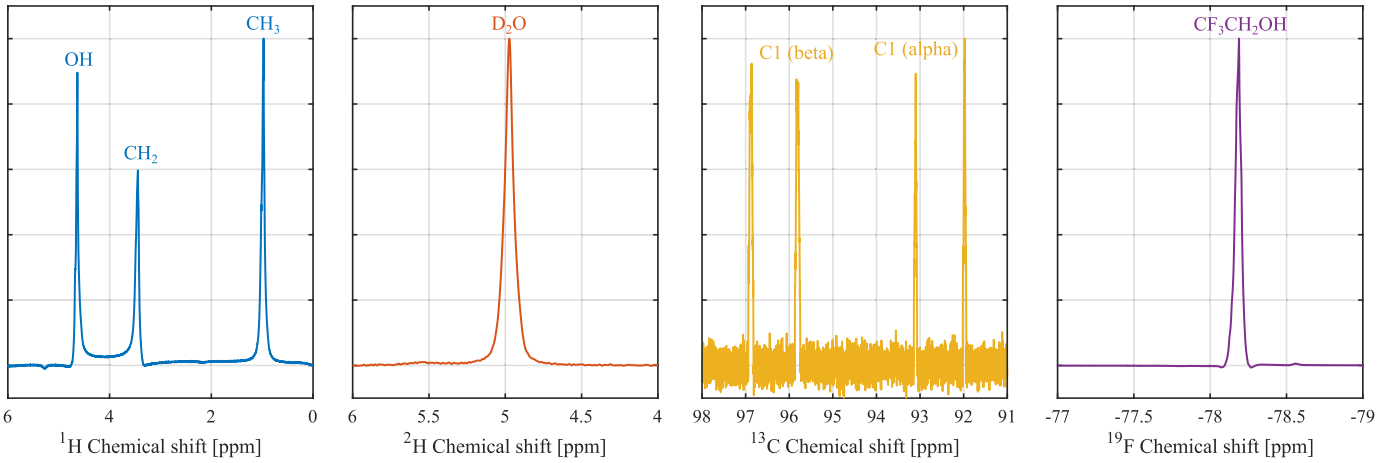

Fig. 17. NMR spectra of ethanol (^{1}H measured with $f_{ref} = 9.3771$ MHz, $N_{div,out} = 64$, and $N_{avg} = 32$), deuterium oxide (^{2}H measured with $f_{ref} = 11.5157$ MHz, $N_{div,out} = 8$, and $N_{avg} = 16$), glucose (^{13}C measured with $f_{ref} = 9.4291$ MHz, $N_{div,out} = 16$, and $N_{avg} = 1000$), and trifluoroethanol (^{19}F measured with $f_{ref} = 8.8295$ MHz, $N_{div,out} = 64$, and $N_{avg} = 32$), obtained with the untuned broadband NMR front-end.

TABLE II
COMPARISON OF STATE-OF-THE-ART ON-CHIP-NMR SYSTEMS

	This work	D. Krüger [27] ESSCIRC'22	H. Bürkle [9] ESSCIRC'21	H. Bürkle [28] ISCAS'20	J. Handwerker [13] ISCAS'17	J. Anders [29] JMR'16	M. Grisi [30] Rev.Sci.Instrum.'15	D. Ha [16] PNAS'14
Magnetic field strength [T]	14.1	0.51	1.13	1.45	7.05	7.05	7.05	0.51
Larmor frequency [MHz]	600/565/151/92	21.8	48	62	300	300	300/282/96/79	21.8
Chip frequency range [MHz]	5 - 780	10 - 60	0.1 - 200	4 - 100	N/A[1]	N/A	1 - 1000	N/A
^{1}H Spin sensitivity [spins/$\sqrt{\text{Hz}}$]	$2.6 \cdot 10^{12}$	N/A	$1.1 \cdot 10^{16}$	$9.2 \cdot 10^{15}$	$3.0 \cdot 10^{13}$	$3.0 \cdot 10^{13}$	$8.0 \cdot 10^{13}$	N/A
^{1}H Spin sensitivity normalized [spins/$\sqrt{\text{Hz}} \cdot \text{T}^2/\text{m}$]	$7.2 \cdot 10^{17}$	N/A	$5.8 \cdot 10^{18}$	$4.9 \cdot 10^{18}$	$4.3 \cdot 10^{18}$	$4.3 \cdot 10^{18}$	$8.8 \cdot 10^{18}$	N/A
Input-referred noise [nV/$\sqrt{\text{Hz}}$]	0.61	0.78	1.1	1.1	N/A	1.3	1.5	0.82
RX gain [dB]	31.5 - 66	30-100	N/A	40	N/A	71	54	34 - 100
TX output voltage [V]	2.5	N/A[2]	50	20	3.3	3.3	2.5	N/A[2]
TX output current [mA_{pp}]	210	580	2000	1400	RX only	RX only	20	502
Technology [µm]	0.13 BiCMOS	0.18 CMOS	0.35 HV	0.35 HV	0.13 CMOS	0.13 CMOS	0.13 CMOS	0.18 CMOS
Chip area [mm^2]	1	5	5.8	7.1	N/A	0.9[3]	1	4
Detection coil	off-chip	off-chip	off-chip	off-chip	on-chip	on-chip	off-chip	off-chip

[1]fixed on-chip tuning to 300 MHz [2]utilizing off-chip RF chokes [3]taken from die micrograph

we used a solution of 20 % ethanol (CH_3-CH_2-OH) in 80% deuterium oxide (^2H_2O or D_2O) to measure ^{1}H and ^{2}H NMR respectively. For the ^{13}C NMR experiments we used 1M D-Glucose-1-^{13}C and for the ^{19}F measurements 2,2,2-trifluoroethanol. Importantly, the noise floor in all these NMR experiments was virtually identical.

C. Comparison With the State-of-the-Art

Table II compares the presented BiCMOS NMR system with the current state-of-the-art in on-chip NMR detectors. To allow for a better comparability with other systems, we normalized the ^{1}H spin sensitivity to the B_0-field and the sensor coil diameter according to [28], neglecting the influence of the skin effect, resulting in a state-of-the-art value of $N_{min,norm} = 7.2 \times 10^{17}$ spins/$\sqrt{\text{Hz}}$ for the presented system.

According to Table II, the presented system achieves a state-of-the-art normalized proton spin sensitivity. Moreover, the presented system achieves a state-of-the-art NMR performance over a large range of frequencies, verified by X-nuclei NMR experiments on four different nuclei, covering a frequency range of more than 6x.

VI. CONCLUSION AND OUTLOOK

In this paper, we have presented a broadband NMR system consisting of a broadband NMR-on-a-chip transceiver and a custom-designed NMR microcoil. The ASIC is manufactured in 0.13 µm BiCMOS and provides an operating frequency from 5 MHz to 780 MHz. Its LNA input stage is optimized for low-noise operation with a large range of different source resistances. Together with the NMR system, we have also presented an extensive noise analysis of the bipolar LNA, including closed-form expressions for the optimum collector current for a given source resistance as well as the optimum source resistance for a given bias current. The system performance and the proposed untuned, broadband readout concept using solenoidal microcoils have been verified in the target NMR application with X-nuclei experiments inside a 14.1 T magnet. The NMR measurements indicate a small loss in SNR in the untuned versus the tuned mode of only 30 %. In the future, we plan to extend the ASIC-based broadband NMR approach to more advanced experiments such as 2D NMR. Furthermore, we plan to use the scalability of the presented ASIC-microil approach to form large-scale arrays of broadband NMR detectors, e.g. for metabolite screening.

REFERENCES

[1] J. Kim, B. Hammer, and R. Harjani, "A 5–300 MHz CMOS transceiver for multi-nuclear NMR spectroscopy," in *Proc. IEEE Custom Integr. Circuits Conf.*, Sep. 2012, pp. 1–4.

[2] J. Anders, F. Dreyer, D. Krüger, I. Schwartz, M. B. Plenio, and F. Jelezko, "Progress in miniaturization and low-field nuclear magnetic resonance," *J. Magn. Reson.*, vol. 322, Jan. 2021, Art. no. 106860.

[3] J. Anders and A. H. Velders, *Microcoils for Broadband Multinuclei Detection*. Hoboken, NJ, USA: Wiley, 2018, ch. 10, pp. 265–296.

[4] R. M. Fratila, M. V. Gomez, S. Sýkora, and A. H. Velders, "Multinuclear nanoliter one-dimensional and two-dimensional NMR spectroscopy with a single non-resonant microcoil," *Nature Commun.*, vol. 5, no. 1, pp. 1–8, Jan. 2014.

[5] J. Anders, F. Dreyer, and D. Krüger, "On-chip nuclear magnetic resonance," in *Handbook of Biochips: Integrated Circuits and Systems for Biology and Medicine*. New York, NY, USA: Springer, 2022, pp. 667–698.

[6] H. Davoodi, M. Jouda, J. G. Korvink, N. MacKinnon, and V. Badilita, "Broadband and multi-resonant sensors for NMR," *Prog. Nucl. Magn. Reson. Spectrosc.*, vols. 112–113, pp. 34–54, Jun. 2019.

[7] Ē. Kupče and T. D. W. Claridge, "New NOAH modules for structure elucidation at natural isotopic abundance," *J. Magn. Reson.*, vol. 307, Oct. 2019, Art. no. 106568.

[8] D. Krüger et al., "A portable CMOS-based spin resonance system for high-resolution spectroscopy and imaging," *IEEE J. Solid-State Circuits*, early access, May 17, 2023, doi: 10.1109/JSSC.2023.3274043.

[9] H. Bürkle, T. Klotz, R. Krapf, and J. Anders, "A 0.1 MHz to 200 MHz high-voltage CMOS transceiver for portable NMR systems with a maximum output current of 2.0 app," in *Proc. IEEE 47th Eur. Solid State Circuits Conf. (ESSCIRC)*, Sep. 2021, pp. 327–330.

[10] S. Hong and N. Sun, "Portable CMOS NMR system with 50-kHz IF, 10-μs dead time, and frequency tracking," *IEEE Trans. Circuits Syst. I, Reg. Papers*, vol. 68, no. 11, pp. 4576–4588, Nov. 2021.

[11] K.-M. Lei et al., "Portable NMR with parallelism," *Anal. Chem.*, vol. 92, no. 2, pp. 2112–2120, Jan. 2020.

[12] J. G. Korvink, N. MacKinnon, V. Badilita, and M. Jouda, "'Small is beautiful' in NMR," *J. Magn. Reson.*, vol. 306, pp. 112–117, Sep. 2019.

[13] J. Handwerker, M. Perez-Rodas, M. Ortmanns, K. Scheffler, and J. Anders, "Towards CMOS-based in-vivo NMR spectroscopy and microscopy," in *Proc. IEEE Int. Symp. Circuits Syst. (ISCAS)*, May 2017, pp. 1–4.

[14] J. Anders, J. Handwerker, M. Ortmanns, and G. Boero, "A fully-integrated detector for NMR microscopy in 0.13 μm CMOS," in *Proc. A-SSCC*, 2013, pp. 437–440.

[15] F. Dreyer, D. Krüger, S. Baas, A. Velders, and J. Anders, "A broadband transceiver ASIC for X-nuclei NMR spectroscopy in 0.13 μm BiCMOS," in *Proc. 20th IEEE Interregional NEWCAS Conf. (NEWCAS)*, Jun. 2022, pp. 65–69.

[16] D. Ha, J. Paulsen, N. Sun, Y.-Q. Song, and D. Ham, "Scalable NMR spectroscopy with semiconductor chips," *Proc. Nat. Acad. Sci. USA*, vol. 111, no. 33, pp. 11955–11960, Aug. 2014.

[17] F. Dreyer, Q. Yang, D. Krüger, and J. Anders, "A chip-based NMR relaxometry system for point-of-care analysis," in *Proc. IEEE Biomed. Circuits Syst. Conf. (BioCAS)*, Oct. 2022, pp. 183–187.

[18] D. Krüger, F. Dreyer, M. Kern, and J. Anders, "An S-band EPR-on-a-chip receiver in 0.13 μm BiCMOS," in *Proc. 28th IEEE Int. Conf. Electron., Circuits, Syst. (ICECS)*, Nov. 2021, pp. 1–5.

[19] J. Handwerker et al., "A CMOS NMR needle for probing brain physiology with high spatial and temporal resolution," *Nature Methods*, vol. 17, no. 1, pp. 64–67, Jan. 2020.

[20] A. Sedra, K. Smith, T. Carusone, and V. Gaudet, *Microelectronic Circuits* (Oxford Series in Electrical and Computer Engineering). London, U.K.: Oxford Univ. Press, 2020. [Online]. Available: https://books.google.de/books?id=VlwHygEACAAJ

[21] J. Handwerker et al., "An array of fully-integrated quadrature TX/RX NMR field probes for MRI trajectory mapping," in *Proc. 42nd Eur. Solid-State Circuits Conf. (ESSCIRC)*, 2016, pp. 217–220.

[22] Q. Yang, J. Zhao, F. Dreyer, D. Krüger, and J. Anders, "A portable NMR platform with arbitrary phase control and temperature compensation," *Magn. Reson.*, vol. 3, no. 1, pp. 77–90, May 2022. [Online]. Available: https://mr.copernicus.org/articles/3/77/2022/

[23] J. Anders, P. SanGiorgio, and G. Boero, "An integrated CMOS receiver chip for NMR-applications," in *Proc. IEEE Custom Integr. Circuits Conf.*, Sep. 2009, pp. 471–474.

[24] V. Saggiomo and A. H. Velders, "Simple 3D printed scaffold-removal method for the fabrication of intricate microfluidic devices," *Adv. Sci.*, vol. 2, no. 9, Sep. 2015, Art. no. 1500125.

[25] M. Mompeán, R. M. Sánchez-Donoso, A. de la Hoz, V. Saggiomo, A. H. Velders, and M. V. Gomez, "Pushing nuclear magnetic resonance sensitivity limits with microfluidics and photo-chemically induced dynamic nuclear polarization," *Nature Commun.*, vol. 9, no. 1, pp. 1–8, Jan. 2018.

[26] J. Anders, P. SanGiorgio, and G. Boero, "A quadrature receiver for μNMR applications in 0.13 μm CMOS," in *Proc. ESSCIRC*, 2010, pp. 394–397.

[27] D. Krüger et al., "A portable CMOS-based MRI system with $67 \times 67 \times 83$ μm^3 image resolution," in *Proc. IEEE 48th Eur. Solid State Circuits Conf. (ESSCIRC)*, Sep. 2022, pp. 225–228.

[28] H. Bürkle, K. Schmid, T. Klotz, R. Krapf, and J. Anders, "A high voltage CMOS transceiver for low-field NMR with a maximum output current of 1.4 app," in *Proc. IEEE Int. Symp. Circuits Syst. (ISCAS)*, Oct. 2020, pp. 1–5.

[29] J. Anders, J. Handwerker, M. Ortmanns, and G. Boero, "A low-power high-sensitivity single-chip receiver for NMR microscopy," *J. Magn. Reson.*, vol. 266, pp. 41–50, May 2016.

[30] M. Grisi, G. Gualco, and G. Boero, "A broadband single-chip transceiver for multi-nuclear NMR probes," *Rev. Sci. Instrum.*, vol. 86, no. 4, Apr. 2015, Art. no. 044703.

Frederik Dreyer (Graduate Student Member, IEEE) received the B.Sc. and M.Sc. degrees in electrical engineering from the University of Stuttgart, Germany, in 2015 and 2018, respectively, where he is currently pursuing the Ph.D. degree with the Institute of Smart Sensors. Since 2018, he has been an Academic Staff Member with the Institute of Smart Sensors, University of Stuttgart. His research interests include nuclear magnetic resonance (NMR), mixed-signal integrated circuits, and RF transceiver electronics.

Daniel Krüger (Graduate Student Member, IEEE) received the B.Sc. and M.Sc. degrees in electrical engineering from the University of Stuttgart, Germany, in 2016 and 2018, respectively, where he is currently pursuing the Ph.D. degree with the Institute of Smart Sensors. He is a Research Fellow with the Donhee Ham Laboratory, Harvard University, Cambridge, MA, USA. His current research interests include mixed-signal ICs for nuclear magnetic resonance (NMR), electron spin resonance (ESR), and biomedical applications.

Sander Baas received the B.Sc. and M.Sc. degrees in molecular life sciences from Wageningen University in 2016 and 2018, respectively, where he is currently pursuing the Ph.D. degree in NMR microcoils, NMR hardware development, and photo-CIDNP hyperpolarization. His research interests include affordable and open hardware for analytical chemistry applications.

Aldrik Velders received the Ph.D. degree from Leiden University in 2000. He was trained in inorganic chemistry with Utrecht University, The Netherlands, and the University of Pavia, Italy. After post-doctoral stays in Florence, Italy, working on metalloproteins and medicinal chemistry, he moved back to The Netherlands to the University of Twente to work on supramolecular chemistry and nanotechnology. In 2012, he set up the Chair Group BioNanoTechology, Wageningen University, working on the development of novel nanomaterials, biomedical applications, and various and diverse topics of NMR applications as well as instrumental aspects.

Jens Anders (Senior Member, IEEE) received the master's degree from the University of Michigan, Ann Arbor, MI, USA, in 2005, the Dipl.-Ing. degree from Leibniz University Hannover in 2007, and the Ph.D. degree from École Polytechnique Fédérale de Lausanne (EPFL), Lausanne, Switzerland, in 2011. From 2013 to 2017, he was an Assistant Professor of biomedical integrated sensors with the Institute of Microelectronics, University of Ulm, Ulm, Germany. Since 2022, he has been the Co-Director of the Institute for Microelectronics Stuttgart (IMS CHIPS). He is currently a Full Professor and the Director of the Institute of Smart Sensors, University of Stuttgart, Stuttgart, Germany. He has authored or coauthored several books and book chapters and more than 150 journals and conference papers. His current research interests include circuit design for sensing applications, including materials science and biomedical and quantum sensing. He served as a Program Committee Member for ESSCIRC, ESSDERC, IEEE SENSORS JOURNAL, and ISSCC. He received the 2015 ITG Publication Award, the Best Live Demo Award from the 2017 IEEE SENSORS JOURNAL, the 2019 Helmholtz Center Berlin Technology Transfer Award, and one of the 2020 Sony Europe Research Awards. He was an Associate Editor of the IEEE TRANSACTIONS ON CIRCUITS AND SYSTEMS—II: EXPRESS BRIEFS and the Guest Editor of the IEEE JOURNAL OF SOLID-STATE CIRCUITS and IEEE SOLID-STATE CIRCUITS LETTERS.